



Microstructure and mechanical properties of friction stir processed Al–Mg₂Si alloys

Qing-dong QIN¹, Hong-long ZHAO¹, Juan LI², Ying-zhe ZHANG³, Xiang-dong SU¹

1. Key Laboratory of Light Metal Materials Processing Technology of Guizhou Province, Guizhou Institute of Technology, Guiyang 550003, China;

2. School of Materials and Energy Engineering, Guizhou Institute of Technology, Guiyang 550003, China;

3. 2011 Special Functional Materials Collaborative Innovation Center of Guizhou Province, Guiyang 550003, China

Received 30 December 2019; accepted 4 June 2020

Abstract: The microstructure and mechanical properties of friction stir processed Al–Mg₂Si alloys were studied by TEM and EBSD. The results showed that an increase in the tool rotation speed (300–700 r/min) led to a decrease in the defect area (from 10.5 mm² to zero), whereas the defect area demonstrated the opposite trend (increased to 1.5 mm² from zero) upon further increasing the rotation speed (700–1200 r/min). The types of defects were transformed from tunnel defects to fusion defects as the rotational speed increased. The coarse Mg₂Si dendrites were broken and fine particles (smaller than 10 μm) formed in the weld nugget (WN). The amount of low-angle grain boundaries increased significantly from 57.7% to 83.6%, which was caused by an increase in the content of the deformed structure (from 1.7% to 13.6%). The hardness, ultimate tensile strength (UTS) and elongation were all greatly improved for the weld nugget. The hardness values of the WNs had the following order: R300<R1200<R500<R900<R700. The UTS and elongation had the following order: BM (base material)<R300<R1200<R500<R900<R700. The UTS and the elongation for the WN were increased by one and three times, respectively.

Key words: Al–Mg₂Si alloy; friction stir processing; ultimate tensile strength; microstructural evolution; defect

1 Introduction

As the only stable intermetallic compound in the Mg–Si system, Mg₂Si possesses excellent properties. For example, it has a high hardness similar to Si, a density lower than that of TiAl and good mechanical properties at high temperatures [1]. In particular, Mg₂Si intermetallic compounds can be produced using common casting processes. An aluminum alloy with high Si and Mg contents generates a substantial amount of Mg₂Si during the casting process and is referred to as an Al–Mg₂Si

alloy [2] or Mg₂Si/Al composite [3]. Due to the excellent properties of Mg₂Si, Al–Mg₂Si alloys also present good mechanical properties in applications that require wear and heat resistance at medium/low temperatures. However, the Mg₂Si phase tends to form a coarse dendritic structure during the solidification process of Al or Mg melts [4,5]. In response to this problem, many studies have been performed to modify the Mg₂Si phase to obtain an increased strength and ductility. YU et al [6] studied the modification of an Al–Mg₂Si alloy with Sb+Ca that underwent hot extrusion and T6 treatment where the Mg₂Si was spheroidized. The ultimate

Foundation item: Project (51594011) supported by the National Natural Science Foundation of China; Project ((2017)5633) supported by the Program for the Distinguished Young Scientific Talents of Guizhou, China; Project ((2017)021) supported by the Guizhou Provincial Higher Education Engineering Research Center, China

Corresponding author: Xiang-dong SU, Tel: +86-851-88210967, E-mail: 20150696@git.edu.cn;

Hong-long ZHAO, Tel: +86-851-88210967, E-mail: 20140441@git.edu.cn

DOI: 10.1016/S1003-6326(20)65384-5

tensile strength (UTS) reached 303 MPa. The same research group of WANG et al [7] studied the effects of Sb on the Mg_2Si phase and the UTS of an Al– Mg_2Si alloy after extrusion, where the primary Mg_2Si phase was transformed into a polyhedral shape and the alloy had a UTS of 283 MPa. In addition, other modification elements have been used to modify Al– Mg_2Si alloys [8]. Although these elements changed the morphology of the Mg_2Si phase, the UTS was usually lower than 250 MPa without the extrusion process [9].

Friction stir processing (FSP) is a novel alloy processing technique derived from friction stir welding (FSW) and can modify the microstructure of alloys [10–18]. During FSP, the alloy is forced by a pin, and heat is simultaneously generated via the rotation and friction of the pin and the shoulder on the rotating tool [19]. The alloys being processed undergo severe plastic deformation. Thus, the microstructures of the processed alloys are modified by FSP. FSP can also be used for surface composite fabrication and microstructure homogenization [20,21], for example, to prepare a supersaturated solid solution of an Al–Zn alloy. During multipass FSP, Zn was incorporated into the Al metal due to the friction and extrusion process of the pin and shoulder, forming a supersaturated solid solution.

As mentioned above, the microstructures of an alloy can be refined through the stirring pin during FSP. Al– Mg_2Si alloys are composed of a coarse brittle Mg_2Si dendrites and a tough Al matrix. An improvement in the mechanical properties depends on the elimination of the coarse Mg_2Si dendrites. Fortunately, brittle Mg_2Si dendrites are easily broken by FSP without producing a negative effect on the tough matrix. Therefore, FSP may simultaneously improve the UTS and elongation. In the present work, the evolution of the microstructures and mechanical properties of an Al– Mg_2Si alloy after FSP with different parameters is studied. One of the objectives is to optimize the FSP parameters to improve the UTS and elongation of the alloys. The other is to investigate the microstructural evolution and its influence on the properties. The mechanisms and laws of the microstructural evolution were explored. Additionally, the relationship between the microstructure and performance has also been analyzed.

2 Experimental

The smelting process and composition of the studied Al– Mg_2Si materials were reported in the literature [2]. Commercially pure Al, pure Mg, and A390 alloys were used to prepare Al– Mg_2Si alloys. The pure Al and A390 alloys were melted at 720 °C in a graphite crucible under an air atmosphere in an electric resistance furnace. Then, pure Mg wrapped with aluminum foil was added into the melt. After holding for 10 min at 780 °C, the melts were poured into a preheated steel mold. The compositions of the alloys used herein were determined by direct-reading spectroscopy, as indicated in Table 1. The hardness, UTS and elongation were HB (107.3±2.3), (123.2±4.3) MPa and (1.13±0.93)%, respectively.

Table 1 Composition of Al– Mg_2Si alloy (wt.%)

Mg	Si	Cu	Ti	Fe	Mn	Zn	Al
8.95	8.91	2.23	0.18	0.12	<0.10	0.03	Bal.

FSP was performed by using a FSW machine (SAEM, HT-JM15×100/2, China), and the rotation tool comprised H13 steel with an 8 mm-long tool pin and a 16 mm-wide tool shoulder. A schematic of the rotation tool is shown in Fig. 1, and the end and root diameters were 6 and 8 mm, respectively. The thread pitch was approximately 1 mm. The constant tilt angle of the tool pin was set to be 2.5° with an ~8 mm plunge depth and clockwise-direction rotation during the FSP. The tool travel speed was 60 mm/min. An Al– Mg_2Si alloy plate with a thickness of 1.6 cm was chosen for the FSP. The spindle rotation speed were set to be 300, 500, 700, 900 and 1200 r/min, and the corresponding samples were named as R300, R500, R700, R900 and R1200, respectively.

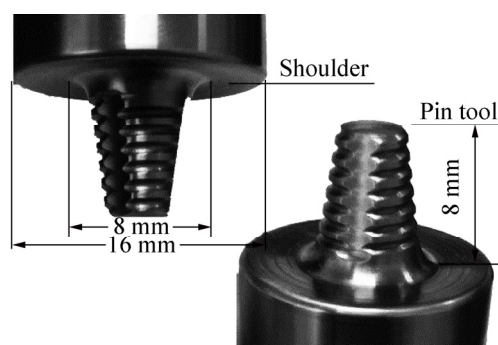


Fig. 1 Sketch of rotation tool

Microhardness tests were performed with a load and an indentation time of 0.2 kg and 10 s, respectively. Five tests were performed for each position. Sketches of the sampling location and dimensions of the tensile samples are shown in Fig. 2. The sampling location was selected in the weld nugget (WN). The length, width and height of the sheet samples used to test performance were 90, 8 and 3 mm, respectively, and the gauge length was 50 mm. The tensile testing was carried out with a crosshead speed of 0.2 mm/min, and four tests were performed for samples with the same parameters.

The samples for microstructural observation were prepared using standard polishing routines, and 0.5 vol.% HF aqueous solution was used as the etchant for optical microscopy (OM) (Zeiss, Axio Observer A1m, Germany) sample preparation. The etch time was 1 s. For EBSD specimen preparation (EDAX, Digiview, USA), the samples were prepared by mechanical grinding and mechanical and electrolytic polishing. The latter was performed using 10% perchloric acid and 90% ethanol solution with a voltage of 16.9 V at room temperature. For the HRTEM (FEI Tecnai G2 F20, USA) survey, the foils were prepared by manual grinding with 5 μm SiC papers, cut into a 4 mm-in-diameter disk and then further thinned by jet electropolishing in a solution of 5% perchloric acid and 95% ethanol at $-50\text{ }^{\circ}\text{C}$.

3 Results and discussion

3.1 Features of macroscopic structure

The surface characteristics of each sample after FSP are shown in Fig. 3, which shows that the processing surfaces were relatively flat and did not contain defects and cracks in the rotation speed range from 300 to 700 r/min. When the speed was increased to 900 r/min (Fig. 3(d)), a crack appeared in the center of the surface; as the rotation speed was further increased to 1200 r/min (Fig. 3(e)), the crack length increased as well. The characteristics of the cross section in the processing zone are shown in Fig. 4.

As expected, the zone consisted of the WN, thermomechanically affected zone (TMAZ), and the base material (BM), similar to the FSW of Al–Mg₂Si materials [2]. In comparison with Fig. 3, although no defects were found on the processing surface at low rotation speeds of 300–700 r/min, the cross-sectional structures show that there was a substantial amount of tunnel defects at the low speed of 300 r/min (defect area $\sim 10.5\text{ mm}^2$), as shown in Fig. 4(a). As the speed was increased to 500 and 700 r/min (Figs. 4(b, c)), the defects disappeared, which was consistent with the results in Fig. 3. As the speed was further increased to 900 and 1200 r/min, the area of the defects increased to 1.5 mm^2 (R1200) with increasing rotation speed, as

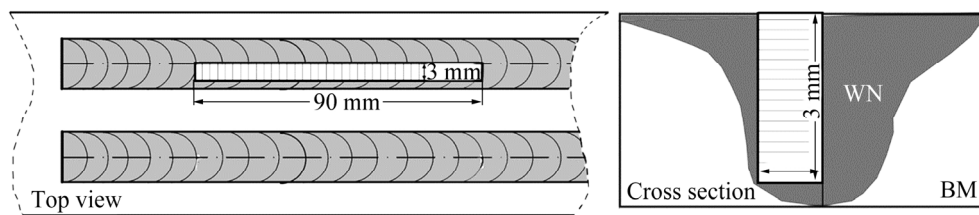


Fig. 2 Sampling locations in joints and dimensions of UTS samples (BM: Base material, WN: Weld nugget)

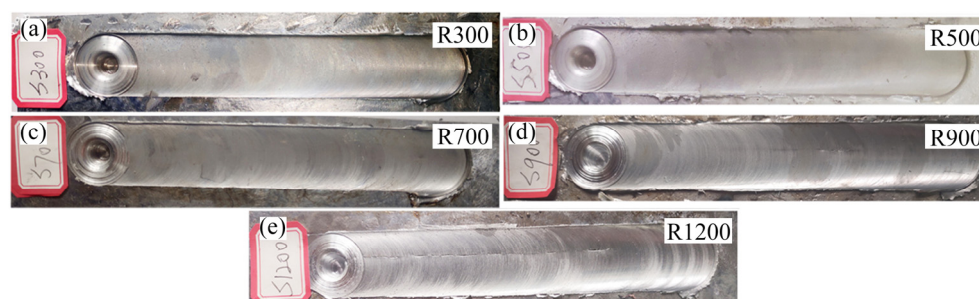


Fig. 3 Characteristics of processing surfaces of samples: (a) R300; (b) R500; (c) R700; (d) R900; (e) R1200

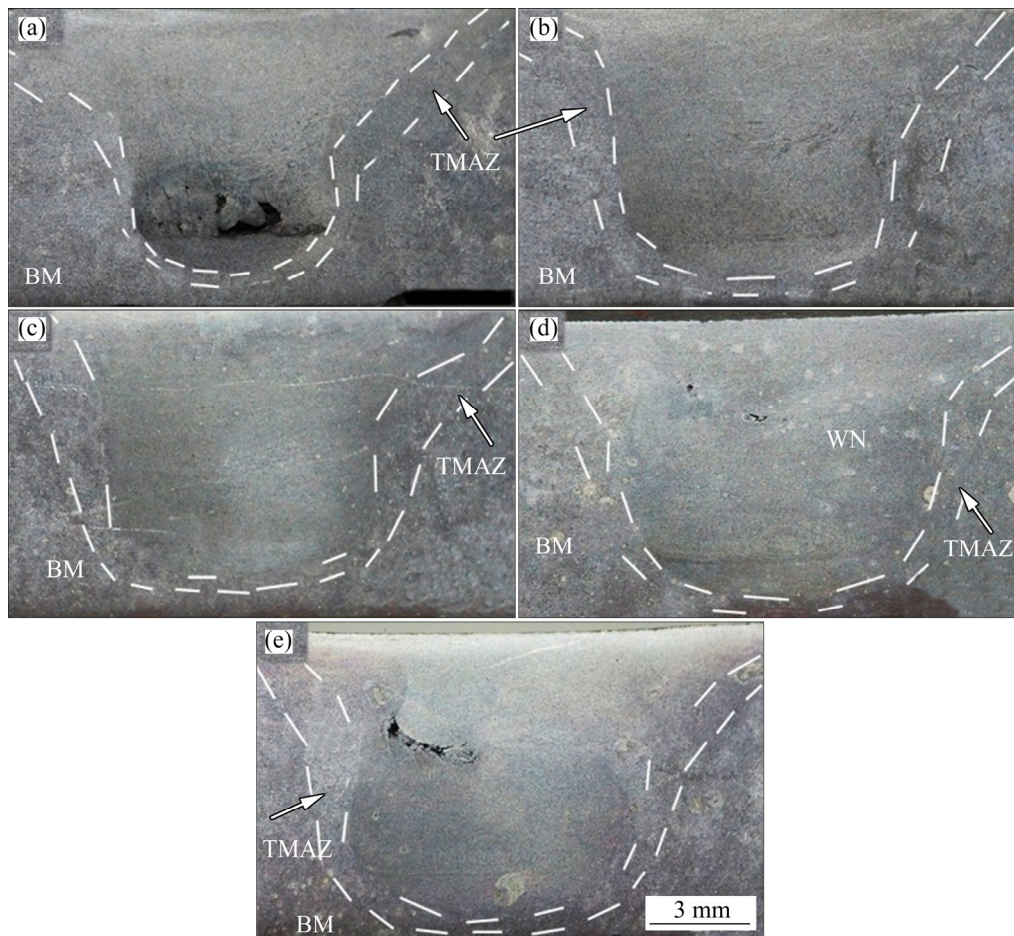


Fig. 4 Cross sectional morphologies in processing zone of samples: (a) R300; (b) R500; (c) R700; (d) R900; (e) R1200

shown in Figs. 4(d, e). Compared with the low speed used for the R300 sample (Fig. 4(a)), the location of the defects migrated from the bottom to the middle and top as the speed was increased.

Usually, an excessive and insufficient heat input can cause defect formation during the FSW process, and the FSP demonstrated a similar phenomenon. A high tool rotation speed can increase the temperature, which increases the fluidity. As a result, the materials migrate from the bottom to the top and leave defects. In contrast, an insufficient heat input during low rotation speeds results in a lack of material fluidity. The materials cannot bond well at the interface, and tunnel defects and voids form at the bottom.

As studied by KIM et al [22] and ELANGO VAN and BALASUBRAMANIAN [23], abnormal stirring is also a factor for defect formation. During FSP, the heat generation and material flow as a result of the stirring are affected by the rotation speed. A high tool rotation speed releases a substantial amount of heat and increases

the temperature in the materials, which increases the fluidity of the material. Due to the high tool rotation speed of the pin, the materials migrate from the bottom to the top and leave defects [23]. However, an insufficient heat input during low-speed rotation results in a lack of material fluidity. A low rotation speed also leads to a lack of mechanical stirring. As a result of these factors, the materials cannot bond well and tunnel defects and voids form. These theoretical analyses are consistent with the phenomena observed in this study. At low rotation speeds, insufficient heating and stirring resulted in a decreased fluidity of the material. In addition, the Al–Mg₂Si materials studied in the present work contained a hard strengthening phase, which led to a substantial decrease in the fluidity. According to the characteristics of FSP, the stirring force at the bottom is the smallest, and near the center of the pins, it is close to zero. Therefore, tunnel defects are generated at the bottom. With increasing rotation speed, the stirring force and temperature increase.

Therefore, the defects disappeared in this study when the speed reached 700 r/min. As the rotation speed was further increased, the excessive stirring and heat caused the defects to reappear, as reported by KIM et al [22]. The upward migration of the defect location showed the characteristics of excessive stirring, i.e., the material migrated from the bottom to the top and left the defects behind [23].

The areas with the defects were tested and analyzed using quantitative analysis software by the Buehler Corporation, as shown in Fig. 5, and the results indicate that upon increasing the rotation speed, the area of the defects rapidly decreased and then slowly increased.

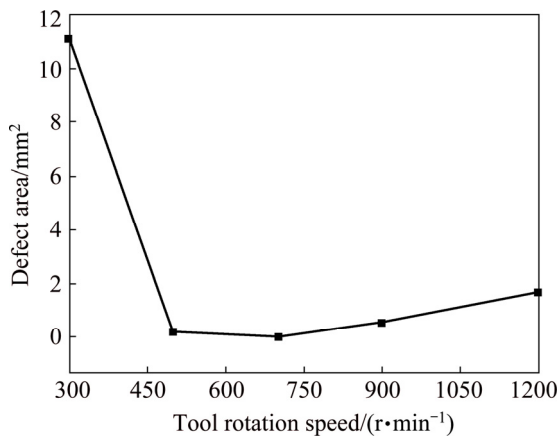


Fig. 5 Relationship between defect area and tool rotation speed determined using quantitative analysis software

3.2 Microstructures of BM, TMAZ and WN

The microstructure of the BM is shown in Fig. 6, where it can be observed that the primary Mg_2Si particles had a polygonal shape with a size of 100 μm (Fig. 6(a)). The eutectic Mg_2Si phase was Chinese script-like or chrysanthemum-shaped, and a small amount of eutectic Si appeared in the form of a sheet (Fig. 6(b)). The microstructural characteristics of the BM are similar to those of previous works by WANG et al [7] and LI et al [8]. With an increase in the volume fraction of Mg_2Si in the Al alloys, the primary Mg_2Si transformed into coarse dendrites, and the Mg_2Si dendrites and the Chinese script-like eutectic Mg_2Si led to a decrease in the UTS and plasticity. Therefore, most of the studies on the modification of the materials involved eliminating the coarse primary and eutectic Mg_2Si phase. FSP can effectively break the dendrites apart by mechanical stirring. After FSP,

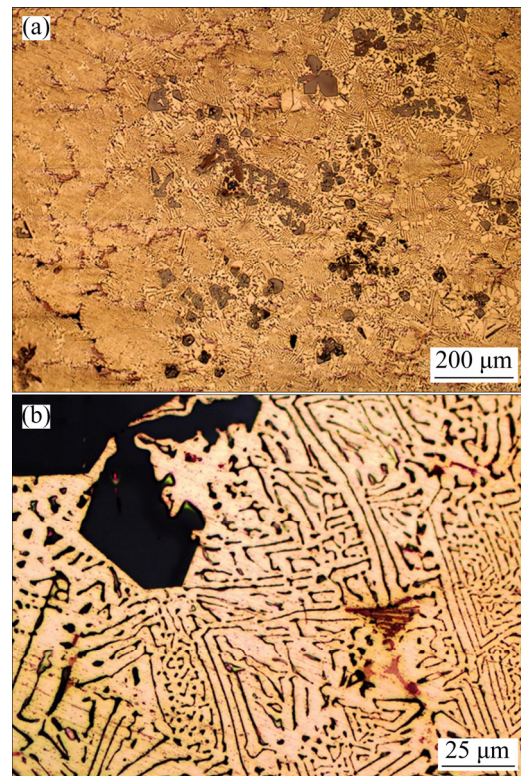


Fig. 6 Microstructures of BM

the microstructure of the WN is shown in Fig. 7. The primary Mg_2Si in each sample transformed into fine particles with a size less than 10 μm . In addition, smaller particles were distributed in the matrix with a size of less than 1 μm . There were two sources for these small particles: one was the broken eutectic Mg_2Si phase, and the other was the broken primary Mg_2Si phase. The change in the primary Mg_2Si particles was not obvious as the rotation speed was increased; however, the fine particles distributing in the matrix changed slightly. With an increase in the rotation speed, the size of the fine particles became more uniform, while the amount also slightly increased. ZHOU et al [24] reported that as the speed was increased, the maximum temperature also increased during FSW. However, when the rotational speed was further increased, the increasing speed of the maximum temperature tended to be slow. Therefore, when the rotation speed was increased to a specific value, the change in the microstructure was not obvious. It can be predicted that the change in the Mg_2Si phase (primary and eutectic) led to an increase in the mechanical properties. Specifically, FSP can obtain better results for the Mg_2Si phase than modification processes with metal elements.

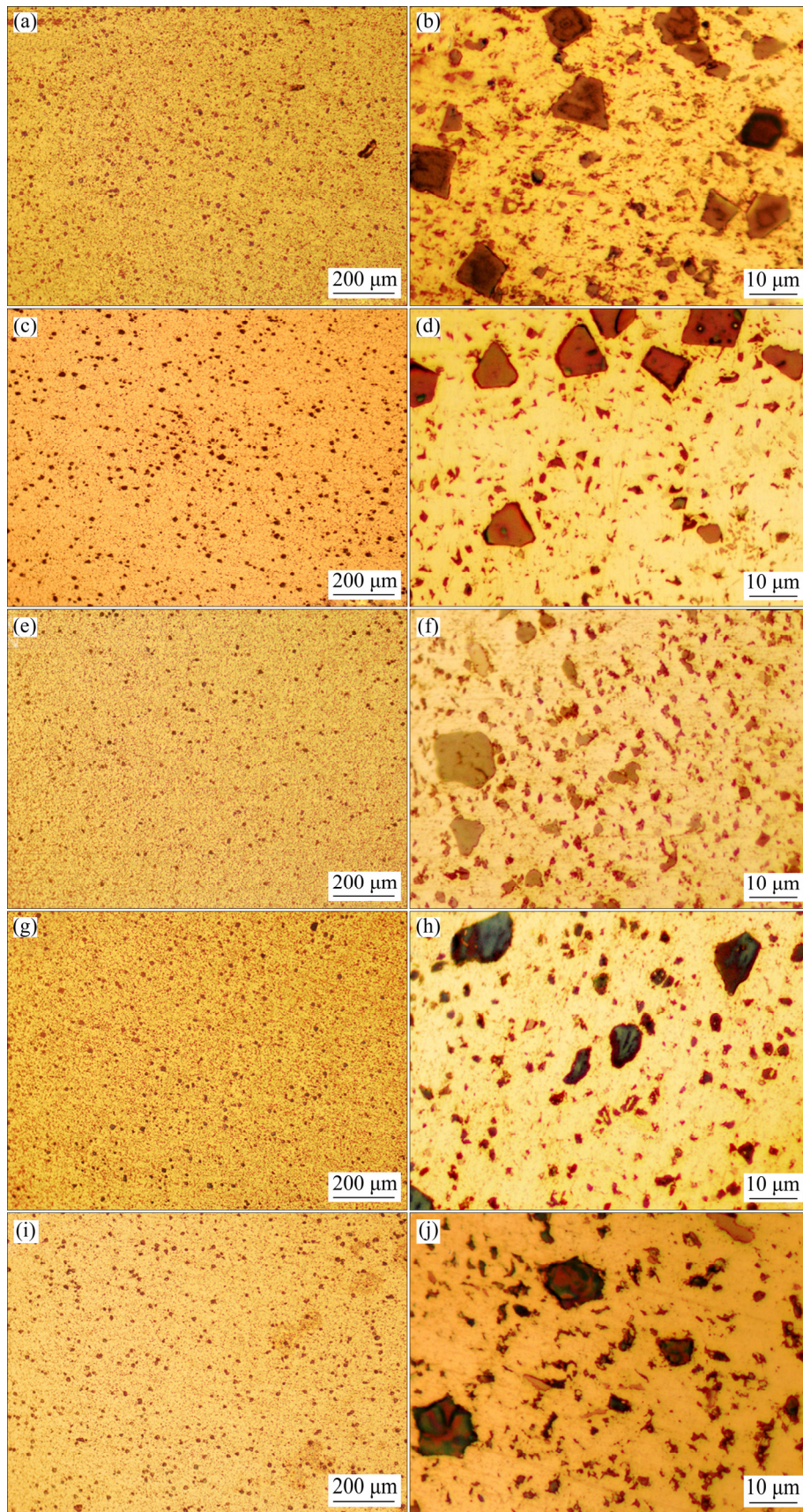


Fig. 7 Microstructures of WN for Al-Mg₂Si materials after FSP: (a, b) R300; (c, d) R500; (e, f) R700; (g, h) R900; (i, j) R1200

The microstructures of the TMAZ are shown in Fig. 8, which correspond to the R300 and R1200 samples, respectively. In the present work, only the TMAZ microstructures with the minimum and maximum rotational speeds (300 and 1200 r/min, respectively) were compared because the microstructure changes were relatively small as the rotational speed was increased. In Fig. 8(a), it can be observed that the width of the TMAZ was 400 μm , and there were still defects in the WN near the TMAZ. Points B and C in Fig. 8(a) lie at the interface of the TMAZ with the BM, and Point B was located in the bottom of the tool pin, where the stirring force was relatively low. The directionality at Point B was not obvious because of the low stirring force. A change in the BM near the TMAZ was also not obvious. Point C was located in the side zone of the tool pin, and the stirring force there was higher than that at Point B. With an increase in the stirring intensity, the eutectic phase in that zone became directional, as shown in Fig. 8(a) and marked by the white arrow in the partially enlarged view. The zone was subject to both extrusion and material flow; as a result, directionality was generated. The BM also showed the characteristics of extrusion. It was clear that the stirring intensity in this area was still much lower than that in the WN; thus, the eutectic phase was not broken. The

microstructure of the TMAZ with a higher rotation speed of 1200 r/min is shown in Fig. 8(b). Macroscopically, there were no significant differences compared to the low rotation speeds, except for fewer defects. The enlarged view of Point B, which was at the interface of the BM and the TMAZ, shows that the directionality of the eutectic phases was very obvious, and its size became finer than that for the low rotation speed (Fig. 8(a)). The BM also had different characteristics. The deformation was substantial, and the directionality was obvious. These phenomena were caused by the high rotation speed and high stirring intensity. As the stirring intensity increased, the temperature and fluidity of the materials increased. The plastic deformation of the BM increased, resulting in the generation of directionality.

When these directional structures are connected to each other, a structure resembling an onion ring shape forms. Onion ring shape structures typically occur during FSP and FSW of Al alloys. The formation of this structure has been studied by many researchers. For example, AMIRIZAD et al [25] believed that onion ring structures are formed by particle-rich bands, geometrical effects and changes in the grain dimensions during the FSW of Al matrix composites. YOON et al [26] found that the generation of onion ring structures in Al alloys was caused by the loads from internal and external screws in the FSW rotation process. YOON et al [26] used a 3D technique and found that the metals began to flow when they were in contact with the probe. The metals flowed down from the upper surface due to the action of the internal screw. The rotation led to a metal flow from the advanced side to the retreated side, and the metals were mixed on the advanced side. Subsequently, the mixed metals were pressed up and into the original zone, and onion ring structures formed. During the continuous rotating flow process, the shape of the onion ring structures was affected by the screws. During FSP, the generation of onion ring structures led to an anisotropy in the mechanical properties, similar to the effect of deformation after hot extrusion.

3.3 Changes in microtextures and misorientation angles

The microtexture can affect the anisotropy of alloys, so the microtexture and misorientation

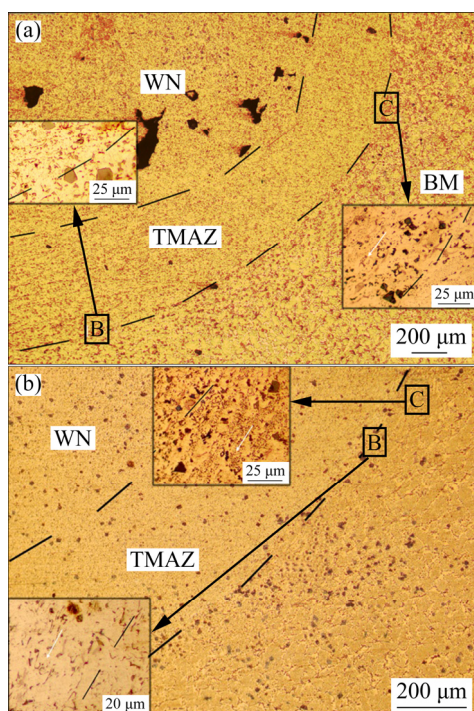


Fig. 8 Microstructures of TMAZ for samples R300 (a) and R1200 (b)

angles (MAs) in sample R700 were studied by EBSD. The EBSD grain boundary and inverse pole figures (IPF) as well as the corresponding MAs of the BM and WN are indicated in Fig. 9. In addition to the changes in the Mg_2Si particles, it can be seen that the $\alpha(\text{Al})$ matrix was also refined after the FSP. Both the BM and the WN had a special directionality. From the above, it can be seen that the whole structure containing the Mg_2Si and the matrix was all refined after the FSP. The MAs were also obviously changed, as shown in Figs. 9(c, d). The fraction of low-angle grain boundaries (LABs) increased from 57.7% to 83.6% compared to that for the BM and WN, respectively. Here, LABs refer to grain boundaries with MAs of 2° – 15° , whereas high-angle grain boundaries (HABs) have MAs greater than 15° . The proportion of LABs and HABs indicates that both BM and WN had LABs, and FSP led to an increase in LABs for the studied materials. Changes in LABs were also found as a result of FSP of Al alloys by JIANG et al [27].

Dynamic recrystallization and grain boundary migration are the reasons for the transformation of the MAs. According to the EBSD results, the constitution of the crystal structure is shown in

Fig. 10. After FSP, the amounts of recrystallized and substructured crystals all decreased, whereas the amount of deformed structure clearly increased. Both of these changes led to a transformation in the MAs. Generally, dynamic recrystallization is a transition process from LABs to HABs, as reported by KAIBYSHEV et al [28], where Al matrix recrystallized after an extrusion process and ultrafine grains were generated. When the material was further strained, the LABs gradually transformed to HABs. Dynamic recrystallization is usually accompanied by the migration of grain boundaries, which is a key factor for the transformation of MAs. During the deformation of an alloy, the material flows along the parallel direction of the rolling plane. This flow causes simultaneous recrystallization and grain boundary migration, which leads to a change in the MAs. In the present work, the FSP reduced the amount of recrystallized structures and a substantial amount of deformed structures formed, which made it the reverse process of dynamic recrystallization. Due to the relatively low temperature during the FSP, this deformed structure did not undergo recrystallization; instead, many LABs formed.

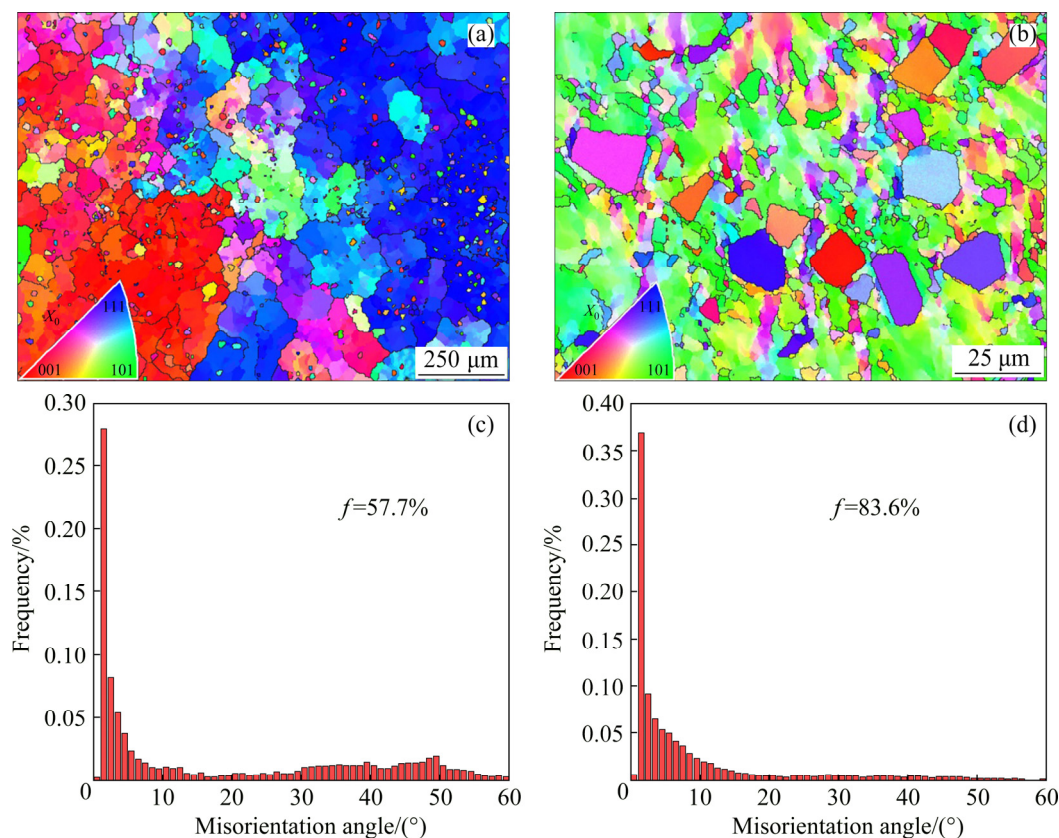


Fig. 9 EBSD images (a, b) and corresponding MAs (c, d) of R700: (a, c) BM; (b, d) WN (f is the volume fraction of LABs)

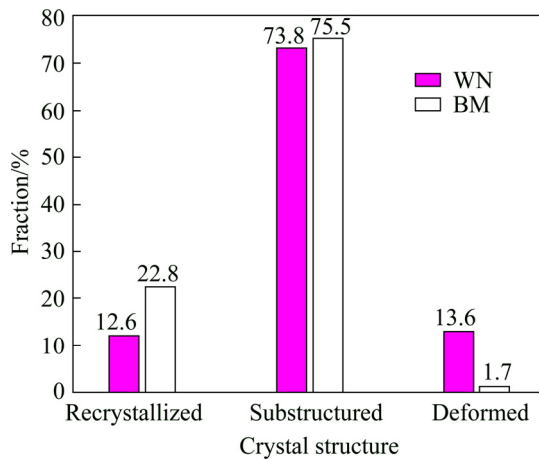


Fig. 10 Constitution of crystal structures in BM and WN after FSP

Figure 11 shows the $\{001\}$ pole figures for the FSP zone and the BM, where Figs. 11(a, b) contain data for the BM and the FSP zone (WN), respectively, and Fig. 11(c) shows the standard $\{001\}$ pole figure for a cubic system. Both the BM and the WN presented obvious microtextures. In the BM, the plate-shaped metal mold led to the generation of directional dendrite growth and a microtexture formed. The microtexture became concentrated in the (101), (212) and $(0\bar{1}1)$ orientations. However, although the WN also had an obvious microtexture, the orientations changed and became concentrated in the (011), (100) and $(0\bar{1}1)$ orientations. It can be observed that the $(0\bar{1}1)$ orientations in the WN were maintained in comparison with the BM, and the intensity of the

microtexture decreased slightly. After FSP, the concentration of the directionality decreased, and the reduction improved the mechanical properties. The maintenance of the $(0\bar{1}1)$ orientation indicates that the FSP mainly produced horizontal deformation and extrusion along the travel direction. This phenomenon is usually found during FSP. SARKARI KHORRAMI et al [29] reported that the microtexture for a severely deformed 1050-Al sheet was $\{001\}$ - (001) and $\{001\}$ - (101) . After FSP, the $\{001\}$ - (101) microtexture was maintained, while the $\{001\}$ - (001) microtexture disappeared. The change in the texture was also affected by the FSP, and the direction and degree of the severe deformation were changed by the FSP. All of these transitions were associated with the mechanical properties.

3.4 Mechanical properties and TEM (HRTEM) analysis

Figure 12 shows the hardness of the materials. The hardness had different values for different rotation speeds. The hardness values of the WNs had the following order: $R300 < R1200 < R500 < R900 < R700$. Although the hardness values of R1200 and R500 were relatively close, the hardness value of R1200 and R300 was lower than that of the BM and the hardness value of R500 was similar to that of the BM. However, the hardness value of R900 and R700 was much higher than that of the BM. Furthermore, the hardness of the TMAZ for all the samples was lower than that for the BM and

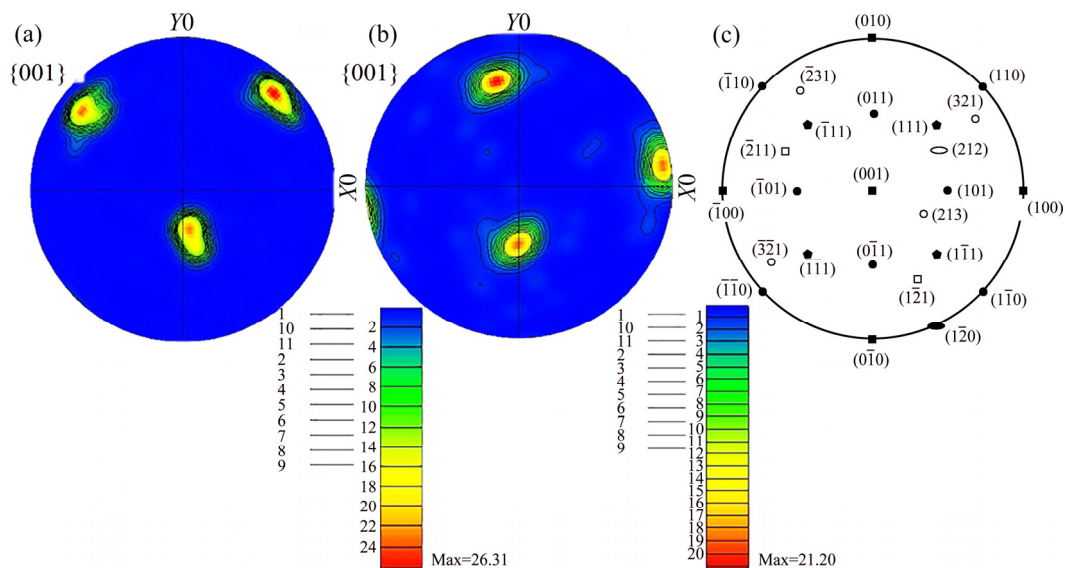


Fig. 11 Pole figures of BM (a) and WN (b), and standard $\{001\}$ pole figure (c)

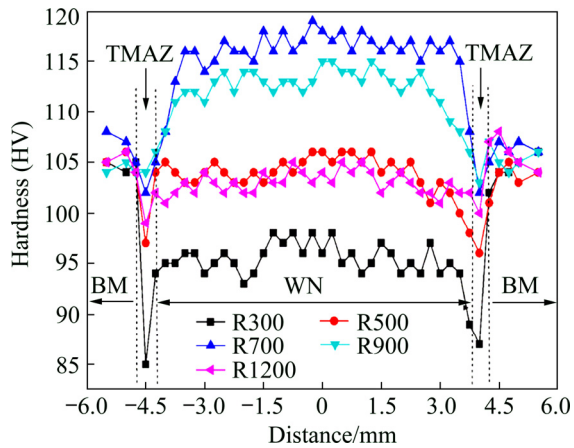


Fig. 12 Hardness of BM and WN in Al-Mg₂Si composites

the WN. The increase in the hardness was caused by two factors: macroscopic and microscopic. Regarding the macroscopic factor, both the low and the high tool rotation speeds (R300 and R1200) produced defects and cavities, and these defects and cavities affected the hardness. Thus, the R300 samples had the lowest hardness values among the

samples in this study. Conversely, an appropriate stirring speed strengthened the matrix by incorporating the broken eutectic phase and the debris of the primary Mg₂Si phase. As a result, the R700 and R900 samples had an increased hardness. The hardness increase in the Al-Mg₂Si materials was found during FSW in previous works by QIN et al [2] and NAMI et al [3]. Microscopic factors also affect the hardness. After FSP, the composition of the precipitates changed. The TEM and HRTEM analysis results for the BM and WN are shown in Fig. 13. In Fig. 13(a), it can be seen that there were needle-shaped β'' precipitates (Mg₅Si₆) and eutectic Mg₂Si, which are marked by black and white arrows, respectively. According to the study by SUNDE et al [30], the needle-shaped β'' phase (Mg₅Si₆) can improve the UTS for common Al alloys, such as 6xxx and 5xxx series alloys, by precipitation strengthening. However, the needle-shaped β'' phase was dissolved by the heat during FSP and a high density of dislocations formed, as shown with the white arrows in Fig. 13(b).

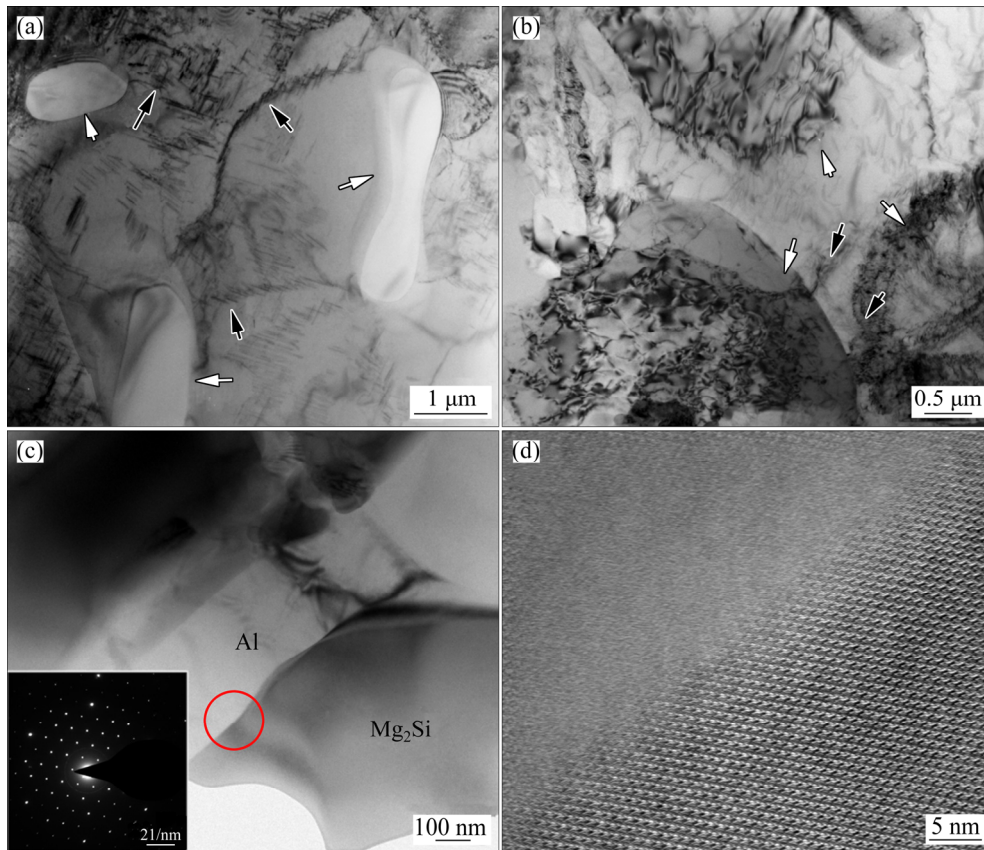


Fig. 13 TEM and HRTEM images of BM and WN in Sample R700: (a) BM; (b) WN; (c) Magnified view of WN; (d) HRTEM image of specified area in (c)

Generally, dissolving phases leads to softening of common Al alloys [26]. In the present work, the softening phenomenon did not occur in the WN due to the existence of strengthening particles in the matrix. However, softening occurred in the TMAZ because the β'' phase disappeared, and the relatively weak stirring did not allow the particles to integrate into the matrix. In addition, a high density of dislocations was evident in the aluminum matrix, as shown in Fig. 13(b).

According to the literature [31], a hot-deformed Al-6063 material contained a high density of dislocation pile-ups at 300 °C at the interface of the dislocations and matrix. When the temperature reached 400 °C, a sufficient number of dislocations caused atomic migration, resulting in subgrain coalescence. Accordingly, the LABs can transform into HABs by absorbing dislocations. During the FSP of the Al–Mg₂Si, the small deformation requires elevated temperatures for atomic migration and grain boundary angle transitions to occur. However, the insufficient heat input during the FSP only caused pile-ups of the high-density dislocations. This also confirms the EBSD results in Figs. 9(c, d). The reinforcement of the Mg₂Si/Al interface bonding is also a factor for hardness improvement, as shown in Figs. 13(c, d). Figure 13(c) shows the interface between Mg₂Si and Al, as well as the selected area electron diffraction pattern of the specified area marked with a red line. The interface was well integrated according to the TEM image. An amorphous transition band formed at the interface, as shown in the HRTEM image in Fig. 13(d). The selected area electron diffraction pattern (Fig. 13(c)), consisting of diffraction spots from the crystal phase and a halo and ring from the amorphous phase, also proved the existence of the amorphous band. These

features improved the mechanical properties.

The tensile samples and the UTS and elongation values of the WN are shown in Fig. 14. The stress–strain curves and fracture surface morphologies are shown in Fig. 15. It is shown in Fig. 14(a) that the Al–Mg₂Si composites did not show necking at each rotation speed because of their low ductility. The tensile test results show that the values of the UTS and elongation varied in a similar type. Both the UTS and elongation values reached a maximum for the R700 sample, while their minimum value occurred for a rotation speed of 300 r/min, as shown in Fig. 14(b). The minimum values for the WN were higher than those for the BM (UTS of 123 MPa and elongation of 1.1%). In particular, the strength and plasticity of sample R700 were significantly improved compared to those for the BM, in which the UTS and the elongation increased by one times and three times, respectively.

The stress–strain curves of the Al–Mg₂Si composite (Fig. 15(a)) show that neither the BM nor the WN presented yield characteristics but fractured after the elastic deformation. The fracture surface morphology of the BM (Fig. 15(b)) is indicative of a brittle fracture surface without typical dimples and shear lips, and obvious pores were present on the surface, as marked by the white arrow. The coarse primary Mg₂Si phase reduced the elongation. In contrast, the R300 and R700 samples possessed shear bands (Figs. 15(c, d)), especially for the fracture surfaces of R700, which exhibited typical shear bands and fine Mg₂Si particles (Fig. 15(d)). Therefore, R700 had a high elongation. In addition to the relatively coarse Mg₂Si particles, R300 also had cavities (marked by the white arrow in Fig. 15(c)). These factors affected the increase in the elongation.

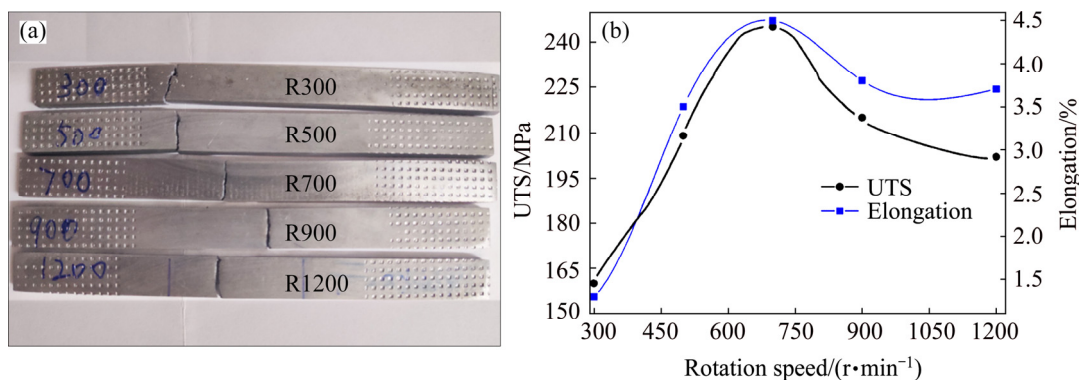


Fig. 14 Tensile samples (a) and tensile properties for WN (b)

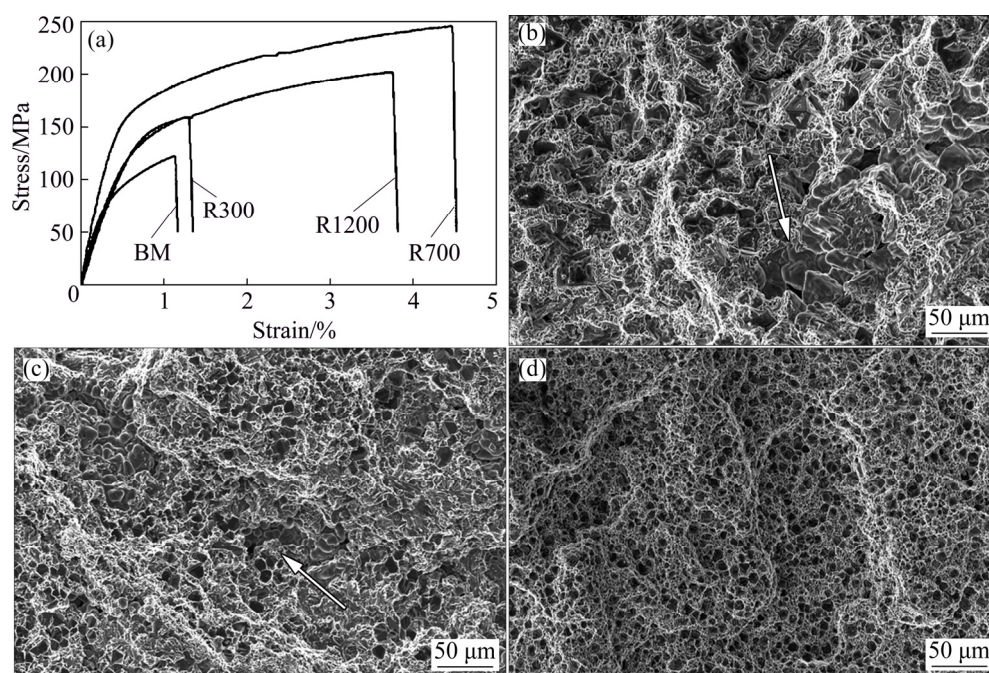


Fig. 15 Stress–strain curves (a) and fracture surface morphologies (b–d) of BM and WN (b) BM; (c) R300; (d) R700

According to the literature [6], the mechanism for the increase is similar to that for the hardness because both are affected by the size of the Mg_2Si , matrix strengthening and defects. The difference is that for a common aluminum alloy, the variations in the strength and ductility are opposite to each other. The special feature for the as-cast Al– Mg_2Si composite is that the coarse Mg_2Si (which contains primary and eutectic phases) caused a simultaneous decrease in the strength and ductility. Therefore, after the FSP with an appropriate rotation speed, the coarse phases were all broken apart, and defects were eliminated, which resulted in an improvement in the strength and ductility. This phenomenon is similar to that of some nanomaterials, as reported by LEI et al [32].

4 Conclusions

(1) For friction stir processed Al– Mg_2Si composite, an increase in the tool rotation speed led to a decrease in the defect area, which disappeared in the range of 300–700 r/min. In the range from 700–1200 r/min, the defects demonstrated the opposite trend.

(2) Tunnel defects and fusion defects corresponded with the low and high rotational speeds, respectively, and the position migrated from the bottom to the top.

(3) In the FSP zone, both primary and eutectic Mg_2Si were broken apart and fine particles formed. The proportion of LABs increased from 57.7% of the BM to 83.6% of the WN. The amount of deformed structure increased from 1.7% to 13.6%.

(4) The hardness, UTS and elongation were greatly improved after FSP. The UTS and elongation increased by one and three times, respectively, for Sample R700.

References

- [1] QIN Qing-dong, ZHAO Yu-guang, LIU Chang, CONG Pei-jun, ZHOU Wei, LIANG Yun-hong. Effect of holding temperature on semisolid microstructure of Mg_2Si/Al composite [J]. *Journal of Alloys and Compounds*, 2006, 416: 143–147.
- [2] QIN Qing-dong, HUANG Bo-wei, WU Yu-jiao, SU Xiang-dong. Microstructure and mechanical properties of friction stir welds on unmodified and P-modified Al– Mg_2Si –Si alloys [J]. *Journal of Materials Processing Technology*, 2017, 250: 320–329.
- [3] NAMI H, ADGI H, SHARIFITABAR M, SHAMABADI H. Microstructure and mechanical properties of friction stir welded Al/ Mg_2Si metal matrix cast composite [J]. *Materials & Design*, 2011, 32: 976–983.
- [4] SHARIFITABAR M, NAMI H. Microstructures of dissimilar friction stir welded joints between 2024-T4 aluminum alloy and Al/ Mg_2Si metal matrix cast composite [J]. *Composites Part B: Engineering*, 2011, 42: 2004–2012.
- [5] ZHENG N, WANG H Y, WANG W, GU Z H, LI D, JIANG Q C. Invalidation of KBF_4 modification on the primary

- Mg₂Si in Mg–Si alloys by Al addition [J]. *Journal of Alloys and Compounds*, 2008, 459: L8–L12.
- [6] YU Hong-chen, WANG Hui-yuan, CHEN Lei, ZHA Min, WANG Cheng, LI Chao, JIANG Qi-chuan. Spheroidization of primary Mg₂Si in Al–20Mg₂Si–4.5Cu alloy modified with Ca and Sb during T6 heat treatment process [J]. *Materials Science and Engineering A*, 2017, 685: 31–38.
- [7] WANG Hui-yuan, LIU Feng, CHEN Lei, ZHA Min, LIU Guo-jun, JIANG Qi-chuan. The effect of Sb addition on microstructures and tensile properties of extruded Al–20Mg₂Si–4Cu alloy [J]. *Materials Science and Engineering A*, 2016, 657: 331–338.
- [8] LI C, WU Y Y, LI H, LIU X F. Morphological evolution and growth mechanism of primary Mg₂Si phase in Al–Mg₂Si alloys [J]. *Acta Materialia*, 2011, 59: 1058–1067.
- [9] QIN Qing-dong, LI Wang-xing, ZHAO Kang-wen, QIU Shi-lin, ZHAO Yu-guang. Effect of modification and aging treatment on mechanical properties of Mg₂Si/Al composite [J]. *Materials Science and Engineering A*, 2010; 527: 2253–2257.
- [10] PADHY G K, WU C S, GAO S. Friction stir based welding and processing technologies–Processes, parameters, microstructures and applications: A review [J]. *Journal of Materials Science & Technology*, 2016, 34: 1–38.
- [11] MA Z Y. Friction stir processing technology: A review [J]. *Metallurgical and Materials Transactions A*, 2008, 39: 642–658.
- [12] ZHAO Hong-yun, YU Ming-run, JIANG Zhi-hua, ZHOU Li, SONG Xiao-guo. Interfacial microstructure and mechanical properties of Al/Ti dissimilar joints fabricated via friction stir welding [J]. *Journal of Alloys and Compounds*, 2019, 789: 139–149.
- [13] ZHOU L, LI G H, ZHANG R X, ZHOU W L, HE W X, HUANG Y X, SONG X G. Microstructure evolution and mechanical properties of friction stir spot welded dissimilar aluminum–copper joint [J]. *Journal of Alloys and Compounds*, 2019, 775: 372–378.
- [14] GENG Pei-hao, QIN Guo-liang, ZHOU Jun, LI Chang-an. Parametric optimization and microstructural characterization of friction welded aeronautic aluminum alloy 2024 [J]. *Transactions of Nonferrous Metals Society of China*, 2019, 29: 2483–2495.
- [15] BARADARANI F, MOSTAFAPOUR A, SHALVANDI M. Effect of ultrasonic assisted friction stir welding on microstructure and mechanical properties of AZ91–C magnesium alloy [J]. *Transactions of Nonferrous Metals Society of China*, 2019, 29: 2514–2522.
- [16] RATHEE S, MAHESHWARI S, SIDDIQUEE A, SRIVASTAVA M. A review of recent progress in solid state fabrication of composites and functionally graded systems via friction stir processing [J]. *Critical Reviews in Solid State and Materials Sciences*, 2018, 43(4): 334–366.
- [17] RATHEE S, MAHESHWARI S, SIDDIQUEE A. Issues and strategies in composite fabrication via friction stir processing: A review [J]. *Materials and Manufacturing Processes*, 2018, 33(3): 239–261.
- [18] RATHEE S, MAHESHWARI S, SIDDIQUEE A, SRIVASTAVA M. Distribution of Reinforcement particles in surface composite fabrication via friction stir processing: Suitable strategy [J]. *Materials and Manufacturing Processes*, 2018, 33(3): 262–269.
- [19] WEGLOWSKI M S. Friction stir processing–State of the art [J]. *Archives of Civil and Mechanical Engineering*, 2018, 18: 114–129.
- [20] HUANG Guo-qiang, HOU Wen-tao, LI Jun-ping, SHEN Yi-fu. Development of surface composite based on Al–Cu system by friction stir processing: Evaluation of microstructure, formation mechanism and wear behavior [J]. *Surface and Coatings Technology*, 2018, 344: 30–42.
- [21] YADAV D, BAURI R, CHAWAKE N. Fabrication of Al–Zn solid solution via friction stir processing [J]. *Materials Characterization*, 2018; 136: 221–228.
- [22] KIM Y G, FUJII H, TSUMURA T, KOMAZAKI T, NAKATA K. Three defect types in friction stir welding of aluminum die casting alloy [J]. *Materials Science and Engineering A*, 2006, 415: 250–254.
- [23] ELANGO VAN K, BALASUBRAMANIAN V. Influences of pin profile and rotational speed of the tool on the formation of friction stir processing zone in AA2219 aluminium alloy [J]. *Materials Science and Engineering A*, 2007, 459: 7–18.
- [24] ZHOU Nan, SONG Dong-fu, QI Wen-jun, LI Xiao-hui, ZOU Ji, ATTALLAH M M. Influence of the kissing bond on the mechanical properties and fracture behaviour of AA5083-H112 friction stir welds [J]. *Materials Science and Engineering A*, 2018, 719: 12–20.
- [25] AMIRIAZD M, KOKABI A H, ABBASI GHARACHEH M, SARRAFI R, SHALCHI B, AZIZIEH M. Evaluation of microstructure and mechanical properties in friction stir welded A356+15% SiC_p cast composite [J]. *Materials Letters*, 2006, 60: 565–568.
- [26] YOON T J, KANG C Y. Observations on metallurgical phenomena and formation of onion ring nugget during friction stir lap welding of dissimilar aluminum by a new 3D technique [J]. *Materials Letters*, 2015, 142: 253–257.
- [27] JIANG H J, LIU C Y, ZHANG B, XUE P, MA Z Y, LUO K. Simultaneously improving mechanical properties and damping capacity of Al–Mg–Si alloy through friction stir processing [J]. *Materials Characterization*, 2017, 131: 425–430.
- [28] KAIBYSHEV R, SHIPILOVA K, MUSIN F, MOTOHASHI Y. Continuous dynamic recrystallization in an Al–Li–Mg–Sc alloy during equal-channel angular extrusion [J]. *Materials Science and Engineering A*, 2005, 396: 341–351.
- [29] SARKARI KHORRAMI M, SAITO N, MIYASHITA Y, KONDO M. Texture variations and mechanical properties of aluminum during severe plastic deformation and friction stir processing with SiC nanoparticles [J]. *Materials Science and Engineering A*, 2019, 744: 349–364.
- [30] SUNDE J K, MARIOARA C D, HELVOORT A T J, HOLMESTAD R. The evolution of precipitate crystal structures in an Al–Mg–Si(–Cu) alloy studied by a combined HAADF-STEM and SPED approach [J]. *Materials Characterization*, 2018, 142: 458–469.

- [31] LIU Yang, GENG Cong, LIN Qi-quan, XIAO Yi-feng, XU Jun-rui, KANG Wei. Study on hot deformation behavior and intrinsic workability of 6063 aluminum alloys using 3D processing map [J]. Journal of Alloys and Compounds, 2017, 713: 212–221.
- [32] LEI Zhi-feng, LIU Xiong-jun, WU Yuan, WANG Hui, JIANG Sui-he, WANG Shu-dao, HUI Xi-dong, WU Yi-dong, GAULT B, KONTIS P, RAABE D, GU Lin, ZHANG Qing-hua, CHEN Hou-wen, WANG Hong-tao, LIU Jia-bin, AN Ke, ZENG Qiao-shi, NIEH T, LU Zhao-ping. Enhanced strength and ductility in a high-entropy alloy via ordered oxygen complexes [J]. Nature, 2018, 563: 546–450.

搅拌摩擦加工 Al-Mg₂Si 合金的显微组织与力学性能

秦庆东¹, 赵宏龙¹, 李娟², 张英哲³, 苏向东¹

1. 贵州理工学院 贵州省轻金属材料制备技术重点实验室, 贵阳 550003;

2. 贵州理工学院 材料与能源工程学院, 贵阳 550003; 3. 贵州省 2011 特种功能材料研究中心, 贵阳 550003

摘要: 通过 TEM 和 EBSD 研究搅拌摩擦加工 Al-Mg₂Si 合金的显微组织和力学性能变化。结果显示: 随着搅拌针转速的增加(300~700 r/min), 缺陷面积逐渐减小(由 10.5 mm² 减小到 0); 当转速进一步增加(700~1200 r/min), 缺陷面积变化又呈相反的趋势(从 0 增加到 1.5 mm²)。在转速的增加过程中, 缺陷的类型从隧道缺陷转变为熔合缺陷。在焊核区, 粗大的 Mg₂Si 枝晶被破碎成细颗粒(<10 μm)。小角度晶界的百分比由 57.7% 增加到 83.6%, 这是由形变组织迅速增加(从 1.7% 到 13.6%)引起的。焊核区的极限抗拉强度(UTS)和伸长率均明显提高, 硬度值按如下顺序增加: R300<R1200<R500<R900<R700, UTS 和伸长率按如下顺序增加: BM(母材)<R300<R1200<R500<R900<R700; 焊核区的 UTS 和伸长率最大值分别增加 1 倍和 3 倍。

关键词: Al-Mg₂Si 合金; 搅拌摩擦加工; 极限抗拉强度; 显微组织演变; 缺陷

(Edited by Bing YANG)